INORGANIC CHEMISTRY FRONTIERS

RESEARCH ARTICLE

View Article Online
View Journal | View Issue



Cite this: *Inorg. Chem. Front.*, 2023, **10**, 6045

# Electron-rich biochar enhanced Z-scheme heterojunctioned bismuth tungstate/bismuth oxyiodide removing tetracycline†

Fuyan Kang,‡[a] Xiaona Jiang,‡[a] Yao Wang,[a] Juanna Ren,[b,c] Ben Bin Xu,[b] Guoyang Gao,[a] Zhanhua Huang *[a] and Zhanhu Guo *[b]

Photocatalytic treatment of antibiotics in aqueous ecosystems has become a promising method. However, the low efficiency photogenerated charge separation and slow kinetics of the catalyst severely limit its deployment for industrial applications. Here, the three-dimensional bismuth tungstate ($Bi_2WO_6$)/bismuth oxyiodide (BiOI) loaded on biochar (BC/BWI) composite catalyst was designed for the efficient removal of tetracycline (adsorption capacity: 227.09 mg $g^{-1}$, removal rate: 99.8%). *Via* construction of Z-scheme heterojunctions at the interface of $Bi_2WO_6$ and BiOI, the built-in electric field promotes the directional separation of photogenerated carriers to achieve efficient separation and utilization of photogenerated charges. Meanwhile, the introduction of electron-rich biochar (BC) effectively enhances the adsorption performance, photogenerated electron migration capacity and mass transfer process of the material. The introduction of BC and the building of Z-scheme heterojunctions effectively achieve the spatially synergistic separation of photogenerated charges. The $^{\bullet}O_2^-$ dominates the photocatalytic process, according to the mechanistic studies. The degradation intermediate product testing revealed that tetracycline is efficiently degraded through two main pathways. This work provides ideas for the design of catalysts for the efficient removal of antibiotics from water bodies.

Received 8th July 2023,
Accepted 4th September 2023

DOI: 10.1039/d3qi01283b

rsc.li/frontiers-inorganic



## 1. Introduction

Tetracycline is the second most used antibiotic in the world and is usually released directly into the environment through human and animal feces.[1–3] Tetracyclines in the environment lead to the emergence of antibiotic-resistant bacteria and antibiotic-resistant genes.[4] The emergence of drug resistance causes a decline in the therapeutic potential of humans and animals.[5,6] According to statistics, 0.7 million people die each year due to antibiotic resistance. Meanwhile, this number will increase to 10 million with the continuous rise in the use of antibiotics in 2050.[7] In addition, tetracycline in water ecosystems will affect the ecological balance, which in turn will seriously affect the environment.[8–10] In the face of current antibiotic pollution, finding an efficient and green water treatment method has become the key to address these problems.

Among the reported many antibiotic and organic removal methods,[11–13] photocatalysis has received widespread attention for its advantages of environmental protection, high efficiency and no secondary pollution.[14–16] $Bi_2WO_6$ stands out in antibiotic removal with its excellent light absorption properties and suitable band gap structure.[17] Many works have demonstrated the excellent performance of $Bi_2WO_6$ in the antibiotic removal process.[18] Construction of heterojunction at the interface can effectively improve $Bi_2WO_6$ properties. $Bi_2WO_6$/BiOI exhibits excellent photocatalytic performance. Construction of heterojunction effectively separates photogenerated charges and reduces the recombination rate of photogenerated carriers.[19] However, the photogenerated charge recombination rate still greatly limits the performance of the catalyst due to carrier recombination during the migration process.

Various biochars have been prepared and applied in energy storage, analysis and other fields.[20–22] The electron-rich biochar can now significantly increase the reactive sites, improve adsorption performance, and accelerate photogenerated electron migration.[23,24] These properties of biochar

[a]*Key Laboratory of Bio-Based Material Science and Technology, Ministry of Education, Material Science and Engineering College, Northeast Forestry University, Harbin 150040, Heilongjiang, China. E-mail: huangzh1975@163.com*
[b]*Mechanical and Construction Engineering, Faculty of Engineering and Environment, Northumbria University, Newcastle Upon Tyne, NE1 8ST, UK. E-mail: zhanhu.guo@northumbria.ac.uk*
[c]*College of Materials Science and Engineering, Taiyuan University of Science and Technology, Taiyuan, 030024, China*

†Electronic supplementary information (ESI) available. See DOI: https://doi.org/10.1039/d3qi01283b

‡These authors contributed equally.

make it a suitable carrier for photocatalysts. To address the problems of low photogenerated charge separation and slow reaction kinetics, the construction of heterojunctions[25] and the introduction of electron-rich biochar became the solution strategy.[26]

In order to achieve effective separation of photogenerated charges and increase the reaction kinetics, a space charge synergistic separation strategy was created. BC/BWI composites were prepared by the calcination method and solvothermal method. Photocatalytic removal of tetracycline shows excellent performance. The Z-scheme heterojunctions at the interface of $Bi_2WO_6$ and BiOI were constructed for the effective separation of photogenerated charges while the built-in electric field promoted the directional migration of photogenerated carriers. The introduction of electron-rich biochar effectively increases the active site and adsorption performance, accelerates the photogenerated electron migration and increases reaction kinetics. Synergistic charge separation of electron-rich carriers and Z-scheme heterojunctions increase the photocatalytic removal of tetracycline. Mechanistic studies indicated that $^{\bullet}O_2^-$ is the main photoactive species. Analysis of reaction intermediates revealed that tetracycline is mineralized through two main degradation pathways. This research provides promising ideas for designing efficient antibiotic removal.

## 2. Experimental

### 2.1 Materials

Ammonium oxalate (AOM), isopropyl (IPA), dimethyl sulfoxide (DMSO) and benzoquinone (BQ) and potassium hydroxide (KOH) were purchased from Aladdin. Concentrated sulfuric acid (98% $H_2SO_4$), bismuth nitrate pentahydrate ($Bi(NO_3)_3{\cdot}5H_2O$), potassium iodide (KI), sodium tungstate dihydrate ($Na_2WO_4{\cdot}2H_2O$), ethylene glycol ($C_2H_6O_2$) and tetracycline (TC) were obtained from Sinopharm Chemical Reagent Co. Ltd. The corncob was purchased from a local farmer's market with a particle size of 80 mesh.

### 2.2 Synthesis of three-dimensional BC/BWI

BC/BWI was synthesized by a simple solvothermal method. Briefly, 0.5 mmol $Bi(NO_3)_3{\cdot}5H_2O$ and 0.5 mmol $Na_2WO_4{\cdot}2H_2O$ were uniformly dispersed in 15 mL of ethylene glycol and the solution was named A solution. The prepared BiOI was also dispersed in 10 mL of ethylene glycol and noted as solution B. Solution B was then gradually added to solution A, and the mixture was stirred for 30 minutes. Meanwhile, 0.23 g of the prepared biochar (BC) was dispersed in 10 mL of aqueous solution and slowly dropped into the stirred solution. The solution was then put into a hydrothermal reactor and heated to 140 °C, where it reacted for 14 hours. Collecting the precipitate after the reaction washing and drying. The samples prepared with different BiOI (0.05 mmol, 0.1 mmol, 0.15 mmol, 0.2 mmol) additions were denoted as $BC/BWI_{0.1}$, $BC/BWI_{0.2}$, $BC/BWI_{0.3}$, $BC/BWI_{0.4}$. Samples prepared without adding BC were recorded as $BWI_{0.2}$. The samples prepared without the addition of BiOI during the preparation were recorded as BC/BW.

### 2.3 Photocatalytic removal of tetracycline

Tetracycline was used as a pollutant model to evaluate the adsorption-photocatalytic performance of catalysts. Typically, 10 mg of catalyst was distributed in 100 mL of 50 mg $L^{-1}$ tetracycline solution. The adsorption–desorption equilibrium was achieved by stirring for 40 minutes in the dark. The 300 W xenon lamp ($\lambda \geq 420$ nm, Hxuv300 Visref, Beijing China Education Au-light Co) was then turned on to start the photocatalytic degradation process. The photocatalytic degradation time was 60 min, and 3 mL of the solution was filtered at 10 min intervals. UV spectrophotometer is used to detect the tetracycline while the maximum absorption wavelength was 358 nm.

$$K = \ln C_0/C_t \quad (1)$$

$$q_e = (C_0 - C_t) \times V/M \quad (2)$$

$$C\% = \left(1 - \frac{C_t}{C_0}\right) \times 100\% \quad (3)$$

where $K$, $C_0$ and $C_t$ are the degradation rate constants, the concentration of tetracycline at initial and time $t$, respectively. $q_e$, $V$, $M$ and $C$% are adsorption capacity, reaction liquid volume, catalyst mass, and degradation rate, respectively.

### 2.4 Characterization and synthesis

ESI† includes detailed information and photoelectrochemical measurements and synthesis of $Bi_2WO_6$, BC and BiOI.

## 3. Results and discussion

### 3.1 Material structure characterization

In this study, biomass waste corncob was used as raw material to prepare porous biochar (BC) by high temperature carbonization and alkaline activation. $Bi_2WO_6$ and BiOI Z-type heterojunction were constructed on BC surface by hydrothermal method. The synthesis process of BC/BWI is shown in Fig. 1. According to the band structure of $Bi_2WO_6$ and BiOI, the constructed heterojunction is more consistent with the Z-type heterojunction, which can better promote photo-generated charge separation and retain strong oxidation and reduction capabilities. Meanwhile, *in situ* construction of BC/BWI Z-type heterojunction on porous BC can also improve the photocatalytic efficiency, and further convert TC into small molecule substances. In addition, the introduction of electron-rich BC accelerates the reaction mass transfer process, promotes the migration of photogenerated charges and enhances the photocatalytic performance.

Detailed morphology and microstructure studies were conducted on the prepared samples using SEM and TEM. The SEM and TEM images of BC prepared by high-temperature carbonization and alkaline activation methods are shown in Fig. S1(a–f).† The TEM images demonstrate the 2D flat and

 

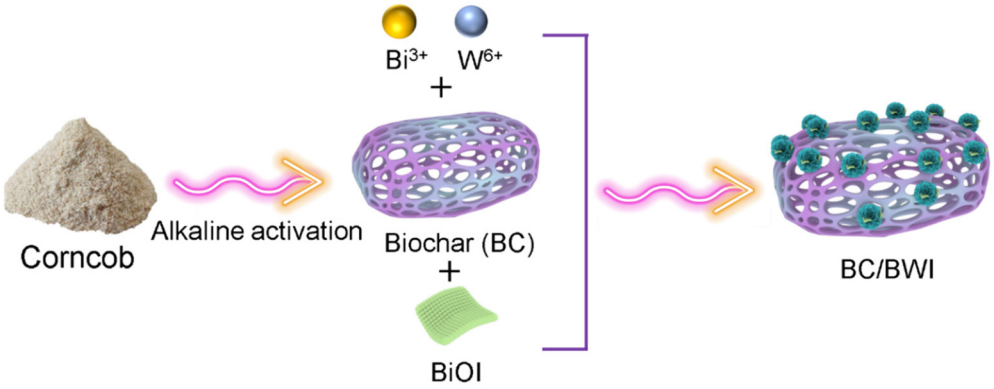


**Fig. 1** Synthesis process of BC/BWI.

thin layered structure of typical biomass carbon materials, which is also an important reason for the increase in specific surface area.[27,28] As shown in Fig. 2a and Fig. S1(g–i),† $Bi_2WO_6$ is a flower like structure formed by crossing a large number of nanosheets. The pure BiOI is assembled from a large number of irregular nanosheets (Fig. 2b), which are loose, rough, and disordered. Fig. 2c shows a BCs/$BWI_{0.2}$ composite catalyst well covered by $Bi_2WO_6$ and BiOI nanofragments. Unlike BC, it is clearly observed that these fragments are more loosely and loosely attached to BC.

To further demonstrate its details, Fig. 2c shows a large and distinct sheet-like structure in the lower part of the image, while the upper part is mostly composed of loose nano fragments with uncovered carbon voids. These findings demonstrated that the production of BiOI is an *in situ* growing process on $Bi_2WO_6$ nanoflowers, which can be regarded as a topological chemical conversion.[29] Due to the abundant attachment points provided by carbon materials, the composite of the two aggregates on BCs forms the structure as shown in the figure. In theory, after adding KI and $Na_2WO_6$ solutions, BiOI is generated in the reaction system. As the reaction progresses, $BiO^+$ is gradually released, and then $BiO^+$ reacts with $WO_4^{2-}$ to generate $Bi_2WO_6$ based on the topological chemical reaction, which is in close contact with the continuously generated BiOI.[30] As a result, a heterostructure was formed between $Bi_2WO_6$ and BiOI, enhancing charge separation in photocatalytic processes. With the increase of KI, $Bi_2WO_6$ nanoflower gradually collapses and decreases, and more and more BiOI is generated. The ideal molar ratio of $Bi_2WO_6$ to BiOI was therefore determined to be 20%, taking into account that stable heterostructures can show excellent photocatalytic performance.

Fig. 2d shows the TEM images of the BC/$BWI_{0.2}$ composite catalyst, and Fig. 2(e and f) shows a locally enlarged view, both

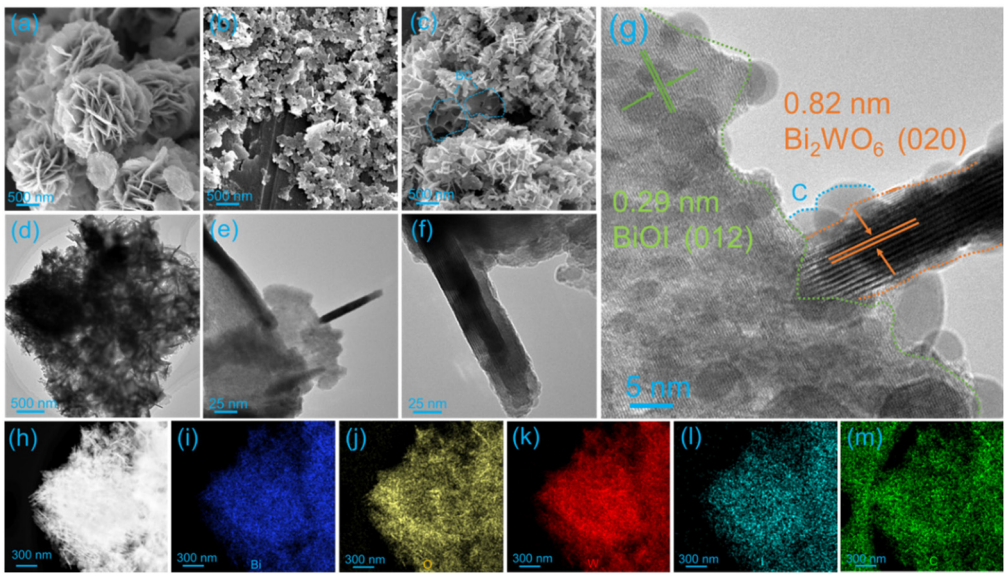


**Fig. 2** SEM images of (a) $Bi_2WO_6$, (b) BiOI, and (c) BC/$BWI_{0.2}$; (d–g) TEM and HR-TEM images of BC/$BWI_{0.2}$; elemental mapping images (h) and (i–m) the element distribution of C, O, W, Bi and I of BC/$BWI_{0.2}$.

of which exhibit distinct spine-like structures. Fig. 2g shows the HR-TEM image of BC/$BWI_{0.2}$. Not only can the carbon edge layer be clearly observed, but also three different sets of lattice stripes can also be clearly observed. The calculated lattice spacing is 0.82 nm and 0.29 nm, respectively. The presence of amorphous carbon layer will effectively promote the separation of photogenerated charges and also serve to enhance the stability of the catalyst.[31] Among them, $d$ = 0.82 nm corresponds to the (020) crystal planes of $Bi_2WO_6$. The $d$ = 0.29 nm is in a better agreement with the (012) crystal planes of BiOI, which further proves the build of a clear heterojunction between $Bi_2WO_6$ and BiOI.[32]

The chemical composition and element content of BCs-$BWI_{0.2}$ composite photocatalyst were analyzed by TEM EDS element mapping (Fig. 2(h–m)), and no other obvious impurities were found. From Fig. 2(i–m), the EDS spectrum of 50% BC/$BWI_{0.2}$ shows strong signals of C, O, W, Bi, and I elements, with a uniform distribution, indicating a high purity of the composite catalyst.

The crystal structure of the BC/BWI was measured, as shown in Fig. 3a. The obvious diffraction peaks at 29.76°, 31.74°, 37.74°, 39.37°, 45.62°, 51.47°, 55.22°, 60.05°, 61.75°, 66.44°, 74.16°, and 75.36°, respectively, belong to the (012), (110), (112), (004), (020), (114), (122), (123), (006), (220), (320), and (130) crystal planes, which are in good agreement with the tetragonal BiOI (JCPDS no. 10-0445).[33] These peaks are mostly sharp, and there are no other strong characteristic diffraction peaks, which proves that BiOI has a high purity and good crystallinity. Also, $Bi_2WO_6$ has a good match to the standard card (JCPDS no. 26-1044). In the BC/BWI of the composite catalyst, the diffraction peaks different from $Bi_2WO_6$, such as (112), (004), and (114), are characteristic diffraction peaks of BiOI with a good crystallinity. Although the peak intensity has decreased, it has not changed its unique crystal structure. More interestingly, as the BiOI content increases, the peak of $Bi_2WO_6$ shifts towards a lower angle (as shown by the red dashed line in the figure). This result effectively proves the doping of $I^-$ in the $Bi_2WO_6$ lattice and the successful *in situ* construction of BWI. The TEM images indicate the successful preparation of the composite catalyst.

The inherent structure and vibration changes of BC, BC/BW, and BC/$BWI_{0.2}$ can be studied through Raman spectroscopy with a scanning range of 50–4000 $cm^{-1}$, as shown in Fig. 3b. For BCs, the detected two typical peaks at 1344 $cm^{-1}$ and 1574 $cm^{-1}$, belong to the two broad peaks of the D-band and G-band of carbon materials.[34] The largest element influencing the degree of carbon graphitization is the relative strength ratio of $I_D/I_G$. The lower the $I_D/I_G$ value, the more graphitization there is. Compared to BC, BC/BW and BC/$BWI_{0.2}$ show decreasing $I_D/I_G$ values. As a result, high-temperature carbonization activation results in the graphitization of biochar, resulting in their transformation from disorder to order and the benign electron conduction in the composite system.

In addition, for BC/BW, the observed three typical peaks of 308, 796, and 830 $cm^{-1}$, correspond to the Bi–W and O–W–O end antisymmetric/symmetric $A_g$ modes of W–O tensile vibration and translational mode, respectively.[35] For BC-$BWI_{0.2}$, apart from the above peak positions, the observed only one peak located at 147 $cm^{-1}$ is attributed to the Bi–I vibration of BiOI.[36] These characterization analyses indicate that the synthesis of BC/$BWI_{0.2}$ catalyst was successful, consistent with the XRD analysis.

The nitrogen adsorption measurement evaluated the specific surface area and pore structure properties. In Fig. 3c, a $H_3$ hysteresis loop type IV with a $P/P_0$ range of 0.8 to 1.0 is clearly visible in BC/BWI.[37] As shown in Fig. 3d, all samples

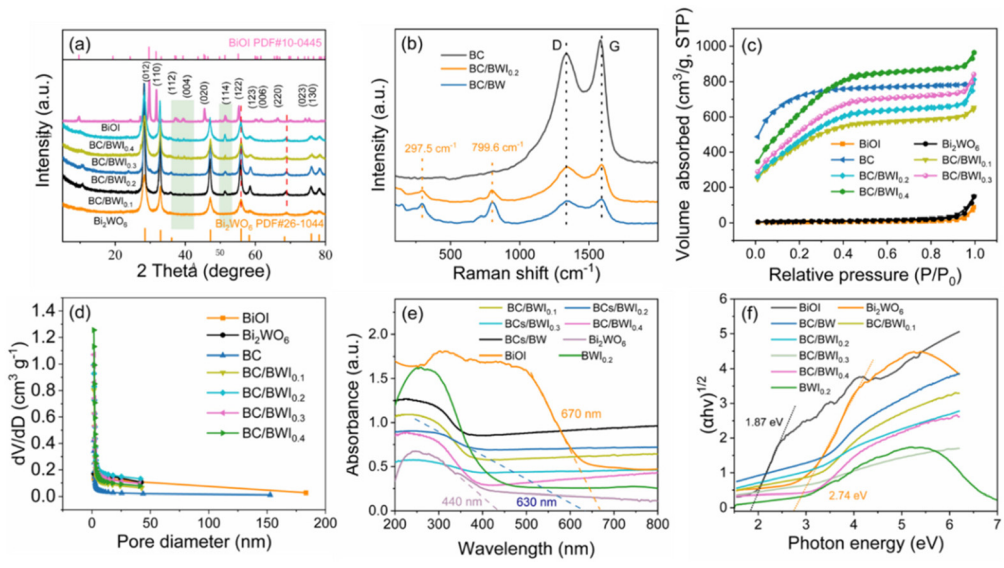


Fig. 3 (a) XRD patterns of $Bi_2WO_6$, BC/$BWI_{0.1}$, BC/$BWI_{0.2}$, BC/$BWI_{0.3}$, BC/$BWI_{0.4}$, and BiOI. (b) Raman shift pattern of BC, BC/BW and BC/$BWI_{0.2}$; (c) the $N_2$ adsorption–desorption isotherms and (d) pore size distribution of samples; (e) UV-vis diffuse reflectance spectra and (f) plot of Kubelka–Munk transformation of samples.

 

prepared in this study have a large number of micropores and mesoporous structures (pore size 0–2 nm). Table S1† shows the physical and chemical properties of materials. It can be seen that the specific surface area of composite $BWI_{0.2}$ is only 64.45 $m^2 \cdot g^{-1}$. When $BWI_{0.2}$ is loaded onto BC, the surface area is significantly increased to 1759.99 $m^2 \cdot g^{-1}$. As the content of BiOI increases, the specific surface area increases, with BC/$BWI_{0.1}$, BC/$BWI_{0.2}$, BC/$BWI_{0.3}$, and BC/$BWI_{0.4}$ being 1215.98, 1759.99, 1962.42, and 2358.99 $m^2 \cdot g^{-1}$, respectively, higher than BC/BW (869.41 $m^2 \cdot g^{-1}$). This means that after partially dense $Bi_2WO_6$ is replaced by loose BiOI, the specific surface area of the composite continues to increase. The larger specific surface area is conducive to carrier migration and provides more active site for the composite catalyst.

Furthermore, more-small sized BiOI fragments enter the pore structure of BC, resulting in a smaller pore size. During the growth process, the composite enters the pores, cross aggregates, and accumulates on the surface of carbon materials, which may be the reason for the increase in pore volume. This will be beneficial for providing more adsorption centers and improving the catalytic performance of the complex.

The UV-Vis diffuse reflectance spectra were tested to examine the series of optical properties of photocatalysts, as shown in Fig. 3e. In the above experiment, the absorption edge of pure $Bi_2WO_6$ was at 440 nm. In Fig. 3e, the light absorption edge of BiOI is about 670 nm, and its absorption ability at wavelengths of 200–800 nm is superior to other samples. Thus the visible light absorption edge was significantly widened by utilizing the special heterojunction structure of the two. The visible light absorption edge of the composite catalyst BC/$BWI_{0.2}$ is about 630 nm, indicating a red shift on the basis of BC/BW, which is conducive to the absorption and utilization of visible light by the photocatalyst. The variation curve of BiOI is shown in Fig. 3f, where BiOI is an indirect transition with $n$ = 1. Therefore, the bandgap of BiOI is 2.02 eV, similar to the reported value in the literature.[38,39] The bandgap of $Bi_2WO_6$ is 2.91 eV, as shown in Fig. 3f. The band gap mainly reflects the characteristics of semiconductors. Low band gaps can promote a relatively low electron excitation energy, and more conductive band electrons can be used for photocatalysis.

The chemical state and surface element composition of BC/$BWI_{0.2}$ composites were studied by XPS, and the results are shown in Fig. 4. As shown in Fig. 4a, only Bi, I, C, W and O elements were found in the of BC/$BWI_{0.2}$ composite material. The peak of C 1s at 284.6 eV can be assigned as the carbon signal used for calibration in the instrument.[40,41] In the spectrum of Bi 4f, as shown in Fig. 4b, the two peaks with binding energies around 163.93 eV and 158.65 eV, in the trivalent oxidation state, correspond to the bimodal signals of Bi $4f_{5/2}$ and Bi $4f_{7/2}$.[42,43] Fig. 4c shows the signal peak of the oxygen element. The binding energy at 529.46 eV and 530.79 eV corresponds to the W–O bond in $Bi_2WO_6$ and the Bi–O bond in $Bi_2O_2$ layered structure respectively. The binding energy at 532.31 eV can be attributed to the $O^{2-}$ anion in $BWI_{0.2}$.[44] The peaks located at 36.96 eV and 34.83 eV correspond to W $4f_{5/2}$ and W $4f_{7/2}$, respectively, and can be divided into $W^{6+}$ oxidation states in the Fig. 4b.

The existence of $Bi_2WO_6$ and BiOI in the catalyst is further supported by the XPS spectrum. It can be seen from Fig. 4e that on the I 3d orbital, a splitting peak appears at the binding energy of about 629.96 eV and 618.48 eV, which belongs to I $3d_{3/2}$ orbital and I $3d_{5/2}$ orbital respectively, confirming the valence state of $I^{-1}$ in the sample.[45] The above results confirm the successful recombination of $Bi_2WO_6$ and BiOI and the possibility of forming heterojunctions, which is consistent with the literature description.[39]

The photocatalytic efficiency mainly depends on the recombination rate of photogenerated charge, as photoluminescence

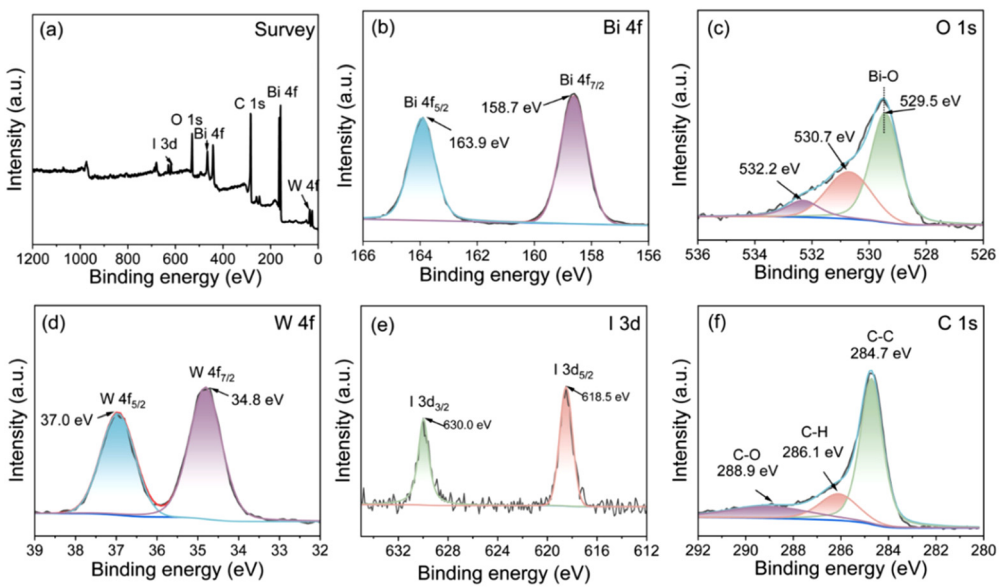


**Fig. 4** (a) XPS full-spectra of 50% BC/$BWI_{0.2}$, XPS high-resolution spectra of (b) Bi 4f, (c) O 1s, (d) W 4f, (e) I 3d and (f) C 1s.

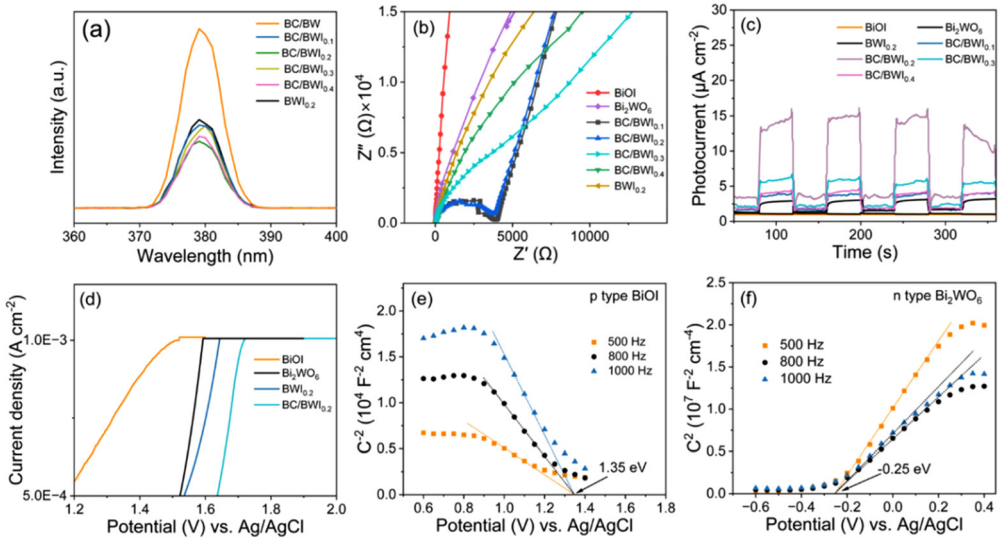


**Fig. 5** (a) PL spectra; (b) Nyquist arc variations; (c) transient photocurrent responses under visible light irradiation; (d) linear sweep voltammetry (LSV) of BC/BWI and Mott–Schottky curve of (e) BiOI and (f) $Bi_2WO_6$.

is caused by the recombination of charge carriers. According to Fig. 5a, the strongest absorption peak of the composite catalyst is at 378 nm. Under the same experimental conditions, the emission intensity of BC/$BWI_{0.2}$ is the lowest, indicating that the introduction of BiOI can significantly promote the separation of photo induced carriers, which can be attributed to the interface electric field.[46] Among them, the emission intensity of BC/$BWI_{0.2}$ is the lowest, significantly improving the separation rate of photo excited carriers. It has been proven that the activity of the BC/$BWI_{0.2}$ catalyst is the strongest.

Fig. 5b shows the EIS Nyquist plot of the prepared sample. The smaller the arc radius in the figure, the higher the carrier transport efficiency in the catalyst.[47] The arc radius of BC/$BWI_{0.2}$ is significantly smaller than that of other samples, supporting the higher photo generated electron and hole separation rate of this composite material. The experimental results are consistent with PL, so it can be predicted that BC/$BWI_{0.2}$ sample may exhibit a higher photocatalytic activity.

Furthermore, the charge separation of the catalyst was characterized using a transient photocurrent response, as shown in Fig. 5c. Under light excitation, an extremely significant photocurrent was generated instantly, and the photocurrent density of BC/BWI for several consecutive cycles was higher than that of other samples. Among them, the photocurrent density of BC/$BWI_{0.2}$ is about 300 times that of the original $Bi_2WO_6$ and 4.5 times that of BC/BW. It has been proven that the electric field between BiOI and $Bi_2WO_6$ is conducive to the separation and transfer of photogenerated charge.

The LSV data demonstrates that BC/BWI has a minimum overpotential, which indicates that BC/BWI can effectively separate photogenerated charges (Fig. 5d). The Mott Schottky method was used to measure the flat band (FB) potential of the catalyst, and Fig. 5(e and f) shows the Mott Schottky plot of BiOI and $Bi_2WO_6$ measured at voltage frequencies of 500, 800 and 1000 Hz. Calculate $E_{FB}$ using the *x*-axis intercept of the linear part of the curve and convert the result into NHE potential. The slope of the Mott Schottky curve indicates that BiOI and $Bi_2WO_6$ are p-type and n-type semiconductors, respectively.[48] Therefore, the $E_{FB}$ of BiOI and $Bi_2WO_6$ are 1.35 eV and −0.25 eV (*vs.* NHE, pH = 7). The above electrochemical analysis well confirms that the introduction of BiOI promotes the improvement of charge separation rate in $Bi_2WO_6$, among which the BC/$BWI_{0.2}$ sample is expected to demonstrate the most excellent photocatalytic performance.

### 3.2 Removal of tetracycline

The adsorption performance of the material will effectively affect the subsequent photocatalytic process and also have a significant role in the removal rate of tetracycline. The adsorption properties of the catalyst were studied using tetracycline as a pollutant model (Fig. 6a). The introduction of BC significantly increases the adsorption performance of the catalyst. The adsorption capacity of BC/$BWI_{0.2}$ is up to 227.09 mg $g^{-1}$ (Table S2†). This reveals that BC not only disperses the catalyst, but also effectively increases the adsorption sites, enhances the mass transfer process of TC molecules, and improves the accessibility of the reaction. On this base, the BC/BWI adsorption kinetics were investigated. The adsorption process of TC is divided into two main stages. In the 30 min, the adsorption process has a large mass transfer driving force because of the high TC concentration in the solution. Meanwhile, during the initial stage of adsorption, the material has a large number of free adsorption sites, allowing TC to adsorb rapidly on the material surface or in the pore structure.[49] The adsorption rate gradually decreases as the adsorption site is occupied and the TC concentration in the solution decreases. At 40 min, the adsorption–desorption process is in dynamic balance.[50] The

 

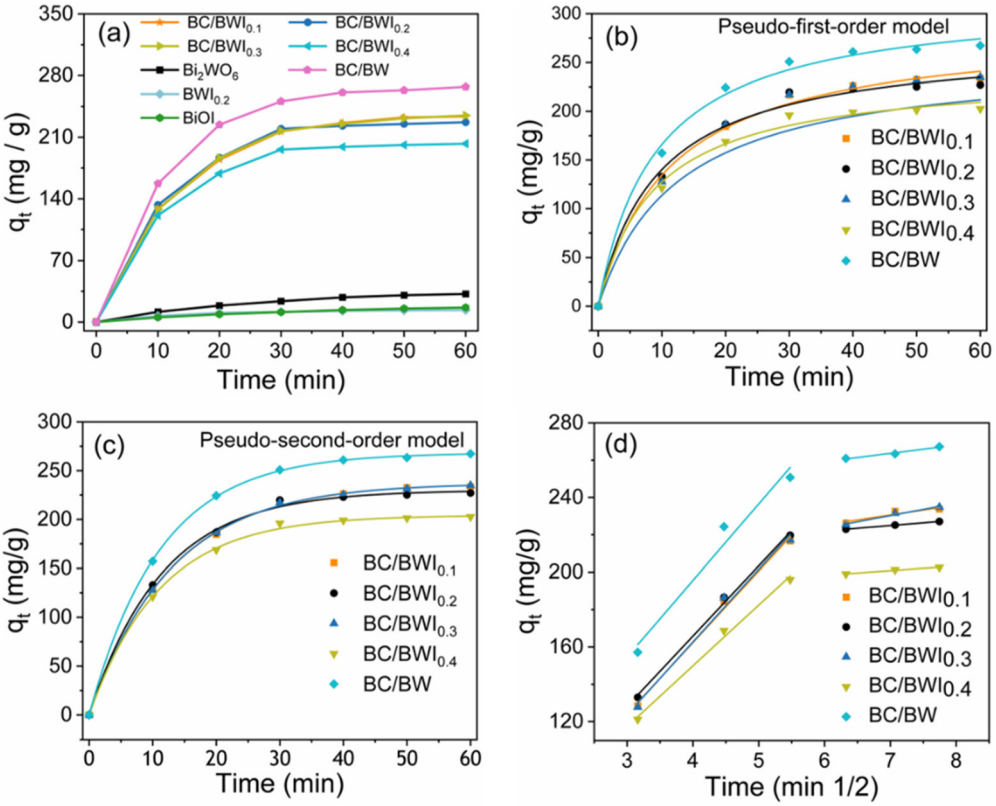


**Fig. 6** (a) BC/BWI adsorption capacity of tetracycline; (b–d) adsorption kinetic fitting.

results of the adsorption kinetic fit are shown in Table S2.† The correlation results indicate that the pseudo-second-order kinetic equation is more appropriate to explain the adsorption method of tetracycline in BC/BWI (Fig. 6b, c and eqn (S1), (S2)†). This reveals that the whole adsorption process may be dominated by chemical adsorption. Also, chemical interactions between the adsorbent and tetracycline may occur through exchange of electrons or sharing of electrons.[51,52] The intra-particle diffusion model was accustomed to describe the adsorption behavior (Fig. 6d and eqn (S3)†). In the first diffusion phase, $K_{\mathrm{dif}\ 1}$ values are relatively large and TC is controlled by molecular diffusion and membrane diffusion. In the second diffusion phase, the $K_{\mathrm{dif}\ 2}$ value is smaller, indicating that TC diffuses from the outer surface of the catalyst into the pore structure. Also, the fitted curve does not pass through the origin. This indicates that the intra-particle diffusion model is not the only rate-controlling mechanism, but that other diffusion mechanisms are also involved in the process.[53]

The photocatalytic degradation performance of 50 mg $L^{-1}$ TC (100 mL) was evaluated through the photocatalytic degradation experiments, and all samples reached adsorption desorption equilibrium after 40 minutes. The experimental data of TC degradation at 420 nm is shown in Fig. 7a. The degradation rate of pure $Bi_2WO_6$ is about 27.53% within 1 hour, and the degradation rate of pure BiOI is about 17.73% within 1 hour. In addition, we also tested that the degradation efficiency of $BWI_{0.2}$ on TC was about 51.84%, which is 1.5 times that of $Bi_2WO_6$ and nearly 3 times that of BiOI. However, it is evident in the figure that the adsorption capacity of $Bi_2WO_6$, BiOI, and $BWI_{0.2}$ is almost zero. With the increase of BC, the adsorption capacity of the composite catalyst for TC is greatly improved. At the same time, the photocatalytic efficiency has also slightly improved, thanks to the fact that BC can serve as receptors for electron migration. The removal rate of TC by $BC/BWI_{0.2}$ is as high as 99.84%, and the removal rate of TC by 50% BC/BW is about 76.05%, further proving that the entry of BiOI can form heterojunctions with $Bi_2WO_6$ to promote photocatalytic activity. The removal rates of TC by $Bi_2WO_6$, BiOI, $BWI_{0.2}$, BC/BW, $BC/BWI_{0.1}$, $BC/BWI_{0.2}$, $BC/BWI_{0.3}$, and $BC/BWI_{0.1}$ were 37.08%, 17.73%, 51.84%, 96.24%, 99.77%, 93.44%, and 90.03%, respectively. According to Fig. 7b, the slopes of the pseudo first order kinetic equation curves $k$ corresponding to the photocatalyst are 6.73, respectively $\times 10^{-3}$, $2.82 \times 10^{-3}$, $1.28 \times 10^{-2}$, $8.16 \times 10^{-2}$, $3.99 \times 10^{-2}$, $8.66 \times 10^{-2}$, $3.07 \times 10^{-2}$ and $2.90 \times 10^{-2}$ $min^{-1}$. The obvious $BCs/BWI_{0.2}$ has better photocatalytic activity, which is consistent with the above characterization results. This work was thoroughly compared with other work (Table S4†). This study shows a significant advantage in the removal of TC, which also proves the efficiency of the space charge synergistic separation.

Stability and repeatability are important evaluation criteria for the practical application of photocatalysts. The cyclic test

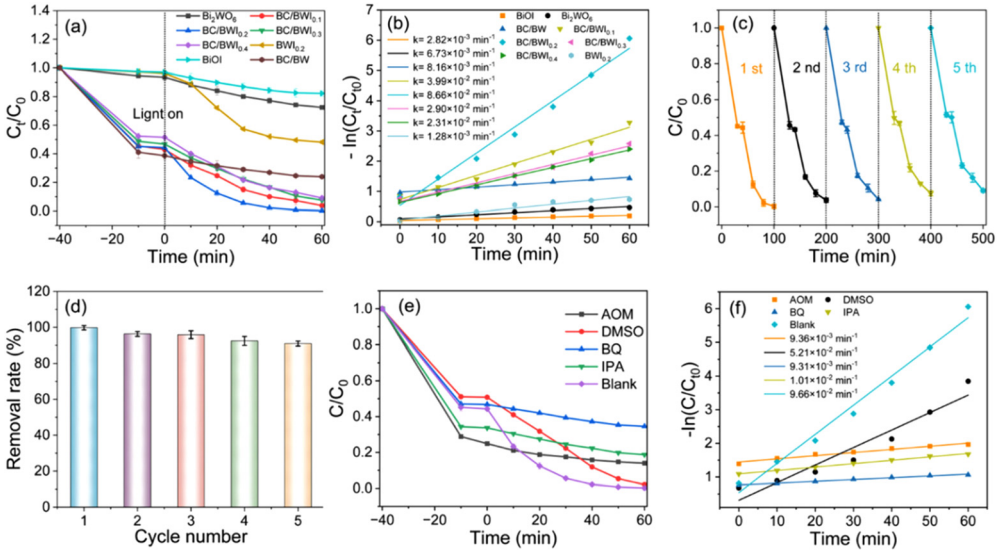


**Fig. 7** (a) Adsorption and degradation curves of TC; (b) kinetics of TC degradation; (c) and (d) reusability of $Bi_2WO_6$ in five runs for TC. (e) and (f) scavenger experiments and kinetic fitting ($t_0$ represents the concentration of TC at the time of illumination).

results in Fig. 7c and d show that the degradation efficiency of BC/$BWI_{0.2}$ has hardly decreased after 5 cycles on TC, which can be applied to practical wastewater treatment fields. On this basis, scavenger experiments were conducted in order to investigate the role of photoactive species. Ammonium oxalate (AOM), dimethyl sulfoxide (DMSO), *p*-benzoquinone (BQ) and isopropanol (IPA) are used as $h^+$, $e^-$, $^{\bullet}O_2^-$ and $^{\bullet}OH$ scavenger respectively. Compared with the blank group, the degradation effect of the experimental group with the addition of trapping agent was reduced to different degrees. The rate constant decreases most significantly with the addition of BQ ($k$ = 9.31 × $10^{-3}$ $min^{-1}$). This indicates that $^{\bullet}O_2^-$ play a dominant role in the photocatalytic degradation of TC.

ESR testing determined the role of active components in the reaction system through DMPO-$^{\bullet}O_2^-$, DMPO-$^{\bullet}OH$, TEMPO-$h^+$, and TEMPO-$e^-$. In the absence of light in Fig. 8(a) and (b), no ESR signal was observed. When BC/$BWI_{0.2}$ and DMPO were mixed under light for 5 and 10 minutes, the characteristic peaks of $^{\bullet}O_2^-$ and $^{\bullet}OH$ both responded and gradually increased. This indicates that in the catalytic system, $^{\bullet}O_2^-$ and $^{\bullet}OH$ were generated under light conditions. As the illumination time increases, the signal intensity of $^{\bullet}O_2^-$ increases more significantly, which is consistent with the results of free radical capture experiments. As shown in Fig. 8(c) and (d), compared to dark conditions, the signal intensity of $e^-$ and $h^+$ decreased significantly within 5–10 minutes under light conditions, indicating the continuous generation of $h^+$ and $e^-$ during the photocatalytic reaction process.

To further understand the degradation process, the TC degradation intermediates were determined by LC-MS. Based on the relevant data (Fig. S2†), we propose two possible degradation pathways. Under light irradiation, BC/BWI produces the strongly oxidizing $^{\bullet}OH$. In pathway I, first, $^{\bullet}OH$ attacks the hydroxyl functional group on the molecule, followed by an oxidation reaction to produce P1 ($m/z$ = 475). Subsequently, the photoactive species generate P2 ($m/z$ = 388) by attacking the ketone and hydroxyl groups on P1. P2 as an unstable intermediate loses its hydroxyl group to further produce P3 ($m/z$ = 318), P4 ($m/z$ = 242) and P5 ($m/z$ = 165).[54] These products then undergo further mineralization reactions to produce $H_2O$ and $CO_2$. In the degradation pathway II, h attacks the benzene ring in TC and introduces hydroxyl and ketone groups to produce P6 ($m/z$ = 459). P6 loses *N*-methyl and further produces P7 ($m/z$ = 415). P7 undergoes a series of reactions such as carbon ring cleavage and loss of hydroxyl group to produce P8 ($m/z$ = 344). P8 undergoes decarboxylation to produce P9 ($m/z$ = 300). P9 undergoes reactions such as dehydroxylation and dealkalization to produce subsequent reaction products (P10, $m/z$ = 246). On this basis, the intermediate products undergo oxidative decomposition and ring opening reactions to produce small molecule products ($H_2O$, $CO_2$ and $NH_4^+$).[55,56] TC is mineralized through both of these pathways to produce small molecule products (Fig. 9).

With these data (Fig. 7 and 8), the generation process of photoactive species is proposed. Under visible light irradiation, the semiconductor undergoes an energy band jump (eqn (4) and (5)). $e^-$ and $h^+$ are produced on the band gap structure of the semiconductor, respectively. Based on the photoelectric characterization data (Fig. 3e, f and 5e, f), $Bi_2WO_6$ and BiOI band gap structures are calculated ($E_{CB1}$ = −0.15 eV and $E_{VB1}$ = 2.59 eV; $E_{CB2}$ = −0.42 eV and $E_{VB2}$ = 1.45 eV). In this case, two heterojunctions may be formed at the semiconductor interface (type II heterojunction and Z-scheme heterojunction).[57] In the type II heterojunction case, the conduction band ($E_{CB2}$) electrons of BiOI will migrate to the conduction band ($E_{CB1}$) of $Bi_2WO_6$. Meanwhile, the holes in the valence band ($E_{VB1}$) of $Bi_2WO_6$ will migrate to the valence band ($E_{VB2}$) of BiOI. The value ($E_{CB1}$ = −0.15 eV) of $E_{CB1}$ is less than

 

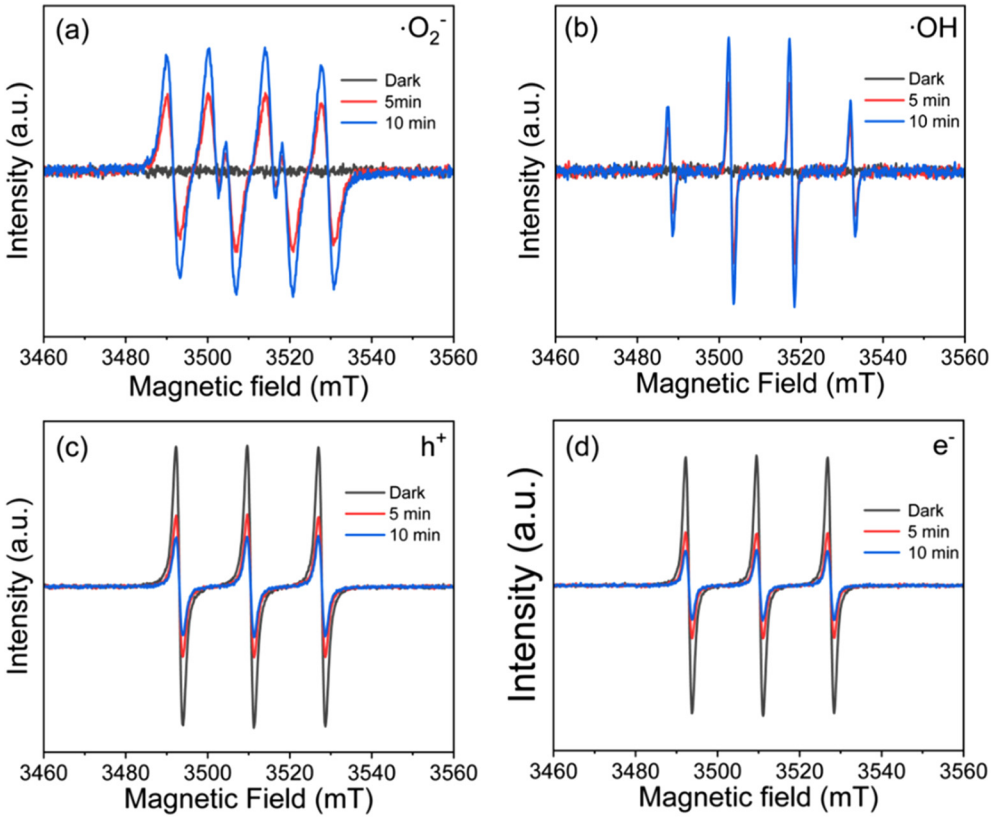


**Fig. 8** ESR spectrum of (a) DMPO-$^{\cdot}O_2^-$; (b) DMPO-$^{\cdot}$OH; (c) TEMPO-$h^+$ and (d) TEMPO-$e^-$ under both the dark and visible light irradiation.

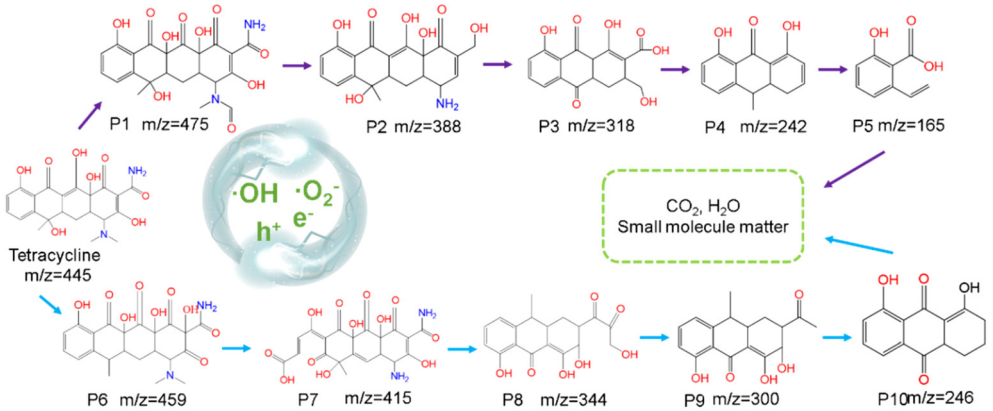


**Fig. 9** BC/BWI photocatalytic degradation of tetracycline pathway.

the generation potential of $^{\cdot}O_2^-$ ($E^{\theta}$ = −0.33 eV). The value ($E_{VB2}$ = +1.45 eV) of $E_{VB1}$ is also greater than the generation potential of $OH^-/^{\cdot}OH$ ($E^{\theta}$ = +1.99 eV) and $H_2O/^{\cdot}OH$ ($E^{\theta}$ = +2.38 eV). The formation of type II heterojunction at the interface is unable to form $^{\cdot}O_2^-$ and $^{\cdot}OH$ in the photocatalytic process, which is not consistent with the experimental reality (Fig. 7e and 8).

$$Bi_2WO_6 + h\nu \rightarrow E_{CB1}(e^-) + E_{VB1}(h^+) \quad (4)$$

$$BiOI + h\nu \rightarrow E_{CB2}(e^-) + E_{VB2}(h^+) \quad (5)$$

$$E_{CB1}(e^-) \rightarrow E_{VB2}(h^+) \quad (6)$$

$$E_{CB2}(e^-) \rightarrow BC \quad (7)$$

$$e^- + O_2 \rightarrow {}^{\cdot}O_2^- \quad (8)$$

$$^{\cdot}O_2^- + H^+ + e^- \rightarrow {}^{\cdot}OH + OH^- \quad (9)$$

$$OH^- + h^+ \rightarrow {}^{\cdot}OH \quad (10)$$

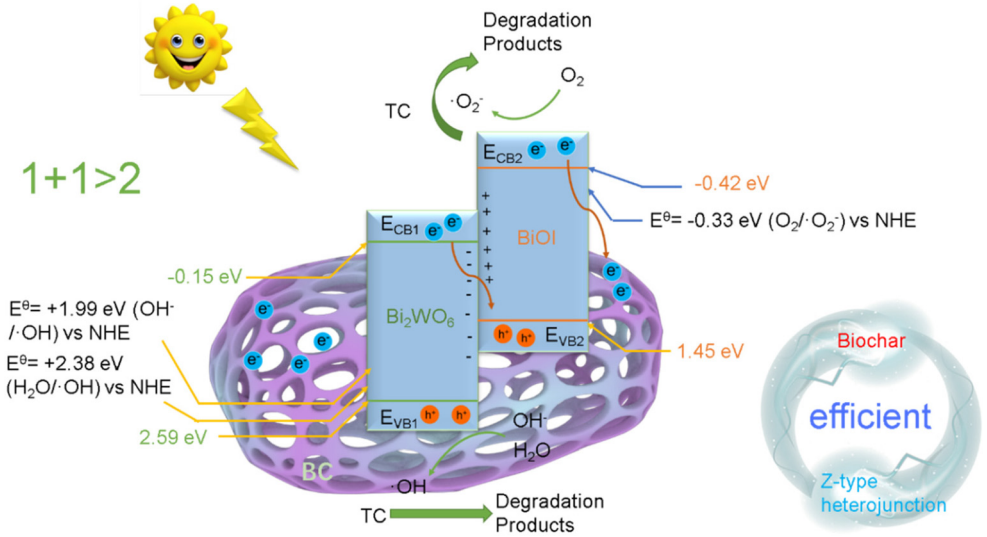


**Fig. 10** Possible path and photocatalytic mechanism of photocatalytic TC degradation by BC/BWI under solar radiation.

$$^{\bullet}OH + TC \rightarrow \text{degradation products} \quad (11)$$

$$^{\bullet}O_2^- + TC \rightarrow \text{degradation products} \quad (12)$$

$$h^+ + TC \rightarrow \text{degradation products} \quad (13)$$

The formation of type II heterojunction is inconsistent with the experimental situation, which indicates that the formation of Z-scheme heterojunction. $E_{CB1}$ electrons leap to $E_{VB2}$ with holes complex (eqn (6)). The photogenerated electrons on $E_{CB2}$ also efficiently migrate to BC. Meanwhile, $E_{VB1}$ and $E_{CB2}$ generate photoactive radicals with environmental factors ($H_2O$ and $O_2$), respectively (eqn (7)–(13)). The formation of Z-scheme heterojunction effectively separates the photogenerated charge and also preserves the redox ability of the material.[58] BC acts as an electron-rich carrier to accelerate the migration of photogenerated electrons and further enhance photocatalytic performance.[59–63] This work introduces electron-rich carriers and constructs Z-scheme heterojunction is to achieve efficient removal of TC. Charge synergistic separation strategy is a favorable idea for designing efficient photocatalysts (Fig. 10).

Based on the above data, the TC removal mechanism is proposed. Under visible light irradiation, the semiconductor material undergoes an energy band jump to produce $e^-$ and $h^+$. Z-scheme heterojunction is formed at the interface of $Bi_2WO_6$ and BiOI. Because the two semiconductor types are different, there is a built-in electric field at the interface. The presence of the built-in electric field promotes the directional migration of photogenerated carriers and accelerates the separation of photogenerated charges. Meanwhile, the introduction of the electron-rich carrier BC increases the adsorption sites of the material and accelerates the mass transfer process of TC. On this basis, BC also effectively promotes the migration of photogenerated electrons and reduces the complex rate of photogenerated charges. Efficient separated photogenerated carriers are involved in the generation of photoactive species. Photoactive species were involved in the degradation of TC, which was generated into small molecule products through two main pathways.

## 4. Conclusions

In summary, the BC/BWI photocatalyst was designed and synthesized with an efficient space charge synergistic separation. BC/BWI shows excellent TC removal performance. The introduction of the electron-rich carrier BC increases the adsorption sites of the material and enhances the mass transfer process of the pollutant molecules. Z-scheme heterojunction achieves an efficient separation of photogenerated carriers, and the built-in electric field promotes the directional migration of photogenerated carriers at the interface. Mechanistic studies have indicated that TC achieves degradation through two main pathways. The $^{\bullet}O_2^-$ plays a dominant role in the photodegradation process. This work provides a rational strategy for designing photocatalysts for efficient photogenerated charge separation. It also exhibits a rational design for the removal of antibiotics in the water ecosystem.

## Conflicts of interest

These authors have no conflict of interest.

## Acknowledgements

This work is financially supported by the National Natural Science Foundation of China (no. 32071713). Meanwhile, the authors would like to gratefully acknowledge the support of National Innovation Training Program of Northeast Forestry University (no. 202210225302).

 

## References


1 Z. Li, W. Xie, F. Yao, A. Du, Q. Wang, Z. Guo and H. Gu, Comprehensive electrocatalytic degradation of tetracycline in wastewater by electrospun perovskite manganite nanoparticles supported on carbon nanofibers, *Adv. Compos. Hybrid Mater.*, 2022, **5**, 2092–2105.

2 Z. Wang, C. W. Wu, Z. Zhang, Y. Chen, W. Y. Deng and W. Q. Chen, Bimetallic Fe/Co-MOFs for tetracycline elimination, *J. Mater. Sci.*, 2021, **56**, 15684–15697.

3 P. Sun, S. Zhou, Y. Yang, S. Liu, Q. Cao, Y. Wang, T. Wågberg and G. Hu, Artificial chloroplast-like phosphotungstic acid—iron oxide microbox heterojunctions penetrated by carbon nanotubes for solar photocatalytic degradation of tetracycline antibiotics in wastewater, *Adv. Compos. Hybrid Mater.*, 2022, **5**, 3158–3175.

4 S. A. R. Ahmadi, M. R. Kalaee, O. Moradi, F. Nosratinia and M. Abdouss, Core–shell activated carbon-ZIF-8 nanomaterials for the removal of tetracycline from polluted aqueous solution, *Adv. Compos. Hybrid Mater.*, 2021, **4**, 1384–1397.

5 C. Lin, B. Liu, L. Pu, Y. Sun, Y. Xue, M. Chang, X. Li, X. Lu, R. Chen and J. Zhang, Photocatalytic oxidation removal of fluoride ion in wastewater by g-$C_3N_4$/$TiO_2$ under simulated visible light, *Adv. Compos. Hybrid Mater.*, 2021, **4**, 339–349.

6 J. Liang, X. Li, J. Zuo, J. Lin and Z. Liu, Hybrid 0D/2D heterostructures: *in situ* growth of 0D g-$C_3N_4$ on 2D BiOI for efficient photocatalyst, *Adv. Compos. Hybrid Mater.*, 2021, **4**, 1122–1136.

7 C. Yu, H. Pang, J.-H. Wang, Z.-Y. Chi, Q. Zhang, F.-T. Kong, Y.-P. Xu, S.-Y. Li and J. Che, Occurrence of antibiotics in waters, removal by microalgae-based systems, and their toxicological effects: A review, *Sci. Total Environ.*, 2022, **813**, 151891.

8 A. J. Gasparrini, J. L. Markley, H. Kumar, B. Wang, L. T. Fang, S. Irum, C. T. Symister, M. Wallace, C. A. D. Burnham, S. Andleeb, N. H. Tolia, T. A. Wencewicz and G. Dantas, Tetracycline-inactivating enzymes from environmental, human commensal, and pathogenic bacteria cause broad-spectrum tetracycline resistance, *Commun. Biol.*, 2020, **3**, 241–253.

9 P. Yanez-Sedeno, M. Pedrero, S. Campuzano and J. M. Pingarron, Electrocatalytic (bio)platforms for the determination of tetracyclines, *J. Solid State Electrochem.*, 2021, **25**, 3–13.

10 J. Shen, Z. Y. Liu, H. N. Yu, J. S. Ye, Y. Long, P. L. Zhou and B. Y. He, Systematic stress adaptation of bacillus subtilis to tetracycline exposure, *Ecotoxicol. Environ. Saf.*, 2020, **188**, 109910.

11 C. Wang, X. Liu, T. Yang, D. Sridhar, H. Algadi, B. Xu, Z. M. El-Bahy, H. Li, Y. Ma, T. Li and Z. Guo, An overview of metal-organic frameworks and their magnetic composites for the removal of pollutants, *Sep. Purif. Technol.*, 2023, **320**, 124144.

12 S. Yang, C. Shi, K. Qu, Z. Sun, H. Li, B. Xu, Z. Huang and Z. Guo, Electrostatic self-assembly cellulose nanofibers/MXene/nickel chains for highly stable and efficient seawater evaporation and purification, *Carbon Lett.*, 2023, DOI: **10.1007/s42823-42023-00540-42820**, in press.

13 Z. Sun, Y. Zhang, S. Guo, J. Shi, C. Shi, K. Qu, H. Qi, Z. Huang, V. Murugadoss, M. Huang and Z. Guo, Confining FeNi nanoparticles in biomass-derived carbon for effectively photo-Fenton catalytic reaction for polluted water treatment, *Adv. Compos. Hybrid Mater.*, 2022, **5**, 1566–1581.

14 Y. Wang, H. Lu, Y. Wang, J. Qiu, J. Wen, K. Zhou, L. Chen, G. Song and J. Yao, Facile synthesis of $TaO_xN_y$ photocatalysts with enhanced visible photocatalytic activity, *RSC Adv.*, 2016, **6**, 1860–1864.

15 Y. Wang, Y. Zhang, H. Lu, Y. Chen, Z. Liu, S. Su, Y. Xue, J. Yao and H. Zeng, Novel N-doped $ZrO_2$ with enhanced visible-light photocatalytic activity for hydrogen production and degradation of organic dyes, *RSC Adv.*, 2018, **8**, 6752–6758.

16 H. Lu, B. Zhao, R. Pan, J. Yao, J. Qiu, L. Luo and Y. Liu, Safe and facile hydrogenation of commercial Degussa P25 at room temperature with enhanced photocatalytic activity, *RSC Adv.*, 2014, **4**, 1128–1132.

17 X. Jiang, S. Chen, X. Zhang, L. Qu, H. Qi, B. Wang, B. Xu and Z. Huang, Carbon-doped flower-like $Bi_2WO_6$ decorated carbon nanosphere nanocomposites with enhanced visible light photocatalytic degradation of tetracycline, *Adv. Compos. Hybrid Mater.*, 2023, **6**, 9.

18 W. Gao, G. Li, Q. Wang, L. Zhang, K. Wang, S. Pang, G. Zhang, L. Lv, X. Liu, W. Gao, L. Sun, Y. Xia, Z. Ren and P. Wang, Ultrathin porous $Bi_2WO_6$ with rich oxygen vacancies for promoted adsorption-photocatalytic tetracycline degradation, *Chem. Eng. J.*, 2023, **464**, 142694.

19 H. Ren, F. Qi, A. Labidi, J. Zhao, H. Wang, Y. Xin, J. Luo and C. Wang, Chemically bonded carbon quantum dots/$Bi_2WO_6$ S-scheme heterojunction for boosted photocatalytic antibiotic degradation: Interfacial engineering and mechanism insight, *Appl. Catal., B*, 2023, **330**, 122587.

20 W. Wang, K. Qu, X. Zhang, M. Teng and Z. Huang, Integrated instillation technology for the synthesis of a pH-responsive sodium alginate/biomass charcoal soil conditioner for controlled release of humic acid and soil remediation, *J. Agric. Food Chem.*, 2021, **69**, 13386–13397.

21 J. Ruan, Z. Chang, H. Rong, T. S. Alomar, D. Zhu, N. AlMasoud, Y. Liao, R. Zhao, X. Zhao, Y. Li, B. B. Xu, Z. Guo, Z. M. El-Bahy, H. Li, X. Zhang and S. Ge, High-conductivity nickel shells encapsulated wood-derived porous carbon for improved electromagnetic interference shielding, *Carbon*, 2023, **213**, 118208.

22 G. Yuan, T. Wan, A. BaQais, Y. Mu, D. Cui, M. A. Amin, X. Li, B. B. Xu, X. Zhu, H. Algadi, H. Li, P. Wasnik, N. Lu, Z. Guo, H. Wei and B. Cheng, Boron and fluorine Co-doped laser-induced graphene towards high-performance micro-supercapacitors, *Carbon*, 2023, **212**, 118101.

23 C. Shi, W. Yuan, K. Qu, J. Shi, M. Eqi, X. Tan, Z. Huang, F. G. Gã¡ndara, D. Pan, N. Naik, Y. Zhang and Z. Guo, Gold/titania nanorod assembled urchin-like photocatalysts with an enhanced hydrogen generation by photocatalytic biomass reforming, *Eng. Sci.*, 2021, **16**, 374–386.

24 S. Yang, K. Qu and Z. Huang, Optimizing hierarchical porous carbon from biomass waste for high-performance supercapacitors, *ES Food Agrofor.*, 2022, **10**, 39–50.

25 C.-Y. Chen and C.-C. Tseng, Two-dimensional $Ga_2S_3$/g-$C_3N_4$ heterojunction composites with highly enhanced photocatalytic activity and stability, *Adv. Compos. Hybrid Mater.*, 2023, **6**, 20.

26 H. Algadi, H. Albargi, A. Umar and M. Shkir, Enhanced photoresponsivity of anatase titanium dioxide ($TiO_2$)/nitrogen-doped graphene quantum dots (N-GQDs) heterojunction-based photodetector, *Adv. Compos. Hybrid Mater.*, 2021, **4**, 1354–1366.

27 Q. Shi, W. Wang, H. Zhang, H. Bai, K. Liu, J. Zhang, Z. Li and W. Zhu, Porous biochar derived from walnut shell as an efficient adsorbent for tetracycline removal, *Bioresour. Technol.*, 2023, **383**, 129213.

28 Y. Sun, C. Liu, Y. Gao, T. Zhang, Y. Jia and S. Wang, All-in-one strategy to prepare molded biochar with magnetism from sewage sludge for high-efficiency removal of Cd(II), *J. Hazard. Mater.*, 2023, **454**, 131488.

29 J. Chen, C. Hu, Z. Deng, X. Gong, Y. Su, Q. Yang, J. Zhong, J. Li and R. Duan, Insight into visible light-driven photocatalytic performance of direct Z-scheme $Bi_2WO_6$/BiOI composites constructed in -situ, *Chem. Phys. Lett.*, 2019, **716**, 134–141.

30 Y. Chu, J. Fan, R. Wang, C. Liu and X. Zheng, Preparation and immobilization of $Bi_2WO_6$/BiOI/g-$C_3N_4$ nanoparticles for the photocatalytic degradation of tetracycline and municipal waste transfer station leachate, *Sep. Purif. Technol.*, 2022, **300**, 121867.

31 D. Li, Y. Fang, J. Lu, J. Sun, X. Zhao, N. Hou and J. Xing, Enhanced biodegradation of PAHs by biochar and a $TiO_2$@biochar composite under light irradiation: Photocatalytic mechanism, toxicity evaluation and ecological response, *Chem. Eng. J.*, 2023, **458**, 141495.

32 F. Zhang, Y. Shao, M. Shu, C. Li and Y. Zheng, Exceptional Photocarriers Separation Efficiency Over $Bi_2WO_6$/BiOI Chemical Bonding Interface for Removal Organic Pollutant, *J. Inorg. Organomet. Polym. Mater.*, 2021, **31**, 3262–3271.

33 G. Gubbiotti, G. Carlotti, L. Giovannini and L. Smardz, Exchange coupling in symmetric Co/Cr/Co trilayer: a Brillouin light scattering study, *Phys. Status Solidi A*, 2003, **196**, 16–19.

34 W. Liang, J. Pan, X. Duan, H. Tang, J. Xu and G. Tang, Biomass carbon modified flower-like $Bi_2WO_6$ hierarchical architecture with improved photocatalytic performance, *Ceram. Int.*, 2020, **46**, 3623–3630.

35 Y. Duan and L. Liu, A double Z-scheme catalyst BiOI/g-$C_3N_4$/$Bi_2WO_6$ for enhanced photocatalytic activity, *J. Chem. Technol. Biotechnol.*, 2023, **98**, 247–256.

36 P. Su, Y. Yang, X. Lu, Y. Zhang, K. Liu and Y. Huang, Synthesis visible photocatalyst carbon/BiOI and its photocatalytic degradation activity, *Inorg. Chem. Commun.*, 2020, **111**, 107643.

37 H. Xu, T. Zhang, D. Wang, D. Cai, S. Chen, H. Wang, S. Shu and Y. Zhu, Degradation of tetracycline using persulfate activated by a honeycomb structured S-doped g-$C_3N_4$/biochar under visible light, *Sep. Purif. Technol.*, 2022, **300**, 121833.

38 L. Kan, C. Chang, Q. Wang and X. Wang, Glycol assisted splitting $BiOIO_3$ into plasmonic bismuth coupled with BiOI co-modified $Bi_2WO_6$ (BiOI/Bi/$Bi_2WO_6$) to form indirect Z-scheme heterojunction for efficient photocatalytic degradation of BPA, *Sep. Purif. Technol.*, 2022, **297**, 121537.

39 X. Y. Kong, W. Q. Lee, A. R. Mohamed and S.-P. Chai, Effective steering of charge flow through synergistic inducing oxygen vacancy defects and p-n heterojunctions in 2D/2D surface-engineered $Bi_2WO_6$/BiOI cascade: Towards superior photocatalytic $CO_2$ reduction activity, *Chem. Eng. J.*, 2019, **372**, 1183–1193.

40 Y. Zhang, X. Li, J. Chen, Y. Wang, Z. Cheng, X. Chen, X. Gao and M. Guo, Porous spherical $Cu_2O$ supported by wood-based biochar skeleton for the adsorption-photocatalytic degradation of methyl orange, *Appl. Surf. Sci.*, 2023, **611**, 155744.

41 C. Zhang, W. Xiong, Y. Li, L. Lin, X. Zhou and X. Xiong, Continuous inactivation of human adenoviruses in water by a novel g-$C_3N_4$/$WO_3$/biochar memory photocatalyst under light-dark cycles, *J. Hazard. Mater.*, 2023, **442**, 130013.

42 S. Wu, J. Sun, Q. Li, Z. D. Hood, S. Yang, T. Su, R. Peng, Z. Wu, W. Sun, P. R. C. Kent, B. Jiang and M. F. Chisholm, Effects of Surface Terminations of 2D $Bi_2WO_6$ on Photocatalytic Hydrogen Evolution from Water Splitting, *ACS Appl. Mater. Interfaces*, 2020, **12**, 20067–20074.

43 X. Yang, Y. Ma, Y. Liu, K. Wang, Y. Wang, M. Liu, X. Qiu, W. Li and J. Li, Defect-Induced Ce-Doped $Bi_2WO_6$ for Efficient Electrocatalytic $N_2$ Reduction, *ACS Appl. Mater. Interfaces*, 2021, **13**, 19864–19872.

44 X. Huang, Q. Guo, B. Yan, H. Liu, K. Chen, S. Wei, Y. Wu and L. Wang, Study on photocatalytic degradation of phenol by BiOI/$Bi_2WO_6$ layered heterojunction synthesized by hydrothermal method, *J. Mol. Liq.*, 2021, **322**, 114965.

45 K. Dou, C. Peng, R. Wang, H. Cao, C. Yao, J. Qiu, J. Liu, N. Tsidaeva and W. Wang, S-scheme tubular g-$C_3N_4$/BiOI heterojunctions for boosting photodegradation of tetracycline and Cr(VI): Mechanism insight, degradation pathway and DFT calculation, *Chem. Eng. J.*, 2023, **455**, 140813.

46 Y. Xiang, P. Ju, Y. Wang, Y. Sun, D. Zhang and J. Yu, Chemical etching preparation of the $Bi_2WO_6$/BiOI p–n heterojunction with enhanced photocatalytic antifouling activity under visible light irradiation, *Chem. Eng. J.*, 2016, **288**, 264–275.

47 L. Wang, K. Xu, W. Cui, D. Lv, L. Wang, L. Ren, X. Xu, F. Dong, S. X. Dou, W. Hao and Y. Du, Monolayer epitaxial heterostructures for selective visible–light–driven photocatalytic NO oxidation, *Adv. Funct. Mater.*, 2019, **29**, 1808084.

48 D. Tantraviwat, A. Nattestad, J. Chen and B. Inceesungvorn, Enhanced photoactivity and selectivity over BiOI-decorated $Bi_2WO_6$ microflower for selective oxidation of benzylamine: Role of BiOI and mechanism, *J. Colloid Interface Sci.*, 2023, **629**, 854–863.

 

49 X. Zhang, D. Zhen, F. Liu, R. Chen, Q. Peng and Z. Wang, An achieved strategy for magnetic biochar for removal of tetracyclines and fluoroquinolones: Adsorption and mechanism studies, *Bioresour. Technol.*, 2023, **369**, 128440.

50 Y. Luo, A. Zheng, J. Li, Y. Han, M. Xue, L. Zhang, Z. Yin, C. Xie, Z. Chen, L. Ji, Z. Hong and X. Xie, Integrated adsorption and photodegradation of tetracycline by bismuth oxycarbonate/biochar nanocomposites, *Chem. Eng. J.*, 2023, **457**, 141228.

51 W. Xiang, X. Zhang, J. Luo, Y. Li, T. Guo and B. Gao, Performance of lignin impregnated biochar on tetracycline hydrochloride adsorption: Governing factors and mechanisms, *Environ. Res.*, 2022, **215**, 114339.

52 J. Tang, Y. Ma, C. Zeng, L. Yang, S. Cui, S. Zhi, F. Yang, Y. Ding, K. Zhang and Z. Zhang, Fe-Al bimetallic oxides functionalized-biochar via ball milling for enhanced adsorption of tetracycline in water, *Bioresour. Technol.*, 2023, **369**, 128385.

53 S. Wang, C. Yuan, F. F. Zafar, M. Wei, F. Marrakchi, B. Cao and Y. Fu, Facile synthesis of chlorella-derived autogenous N-doped porous biochar for adsorption on tetracycline, *Environ. Pollut.*, 2023, **330**, 121717.

54 M. Cai, C. Wang, Y. Liu, R. Yan and S. Li, Boosted photocatalytic antibiotic degradation performance of $Cd_{0.5}Zn_{0.5}S$/carbon dots/$Bi_2WO_6$ S-scheme heterojunction with carbon dots as the electron bridge, *Sep. Purif. Technol.*, 2022, **300**, 121892.

55 E. Avdi, B. J. Hickey, D. Greig, M. A. Howson, M. J. Hall, J. Xu, M. J. Walker, N. Wiser and P. Degroot, Giant Magnetothermopower and giant magnetoresistance in molecular-beam epitaxy-grown Co/Cu(111) superlattices, *J. Appl. Phys.*, 1993, **73**, 5521–5523.

56 J. Niu, Z. Song, X. Gao, Y. Ji and Y. Zhang, Construction of $Bi_2WO_6$ composites with carbon-coated $Cu_2O$ for effective degradation of tetracycline, *J. Alloys Compd.*, 2021, **884**, 161292.

57 L. Su, P. Wang, M. Li, Z. Zhao, Y. Li and S. Zhan, Synergistic enhancement of photocatalytic molecular oxygen activation by nitrogen defect and interfacial photoelectron transfer over Z-scheme α-$Fe_2O_3$/g-$C_3N_4$ heterojunction, *Appl. Catal., B*, 2023, **335**, 122890.

58 Z. Zhang, R. Ji, Q. Sun, J. He, D. Chen, N. Li, H. Li, A. Marcomini, Q. Xu and J. Lu, Enhanced photocatalytic degradation of 2-chlorophenol over Z-scheme heterojunction of CdS-decorated oxygen-doped g-$C_3N_4$ under visible-light, *Appl. Catal., B*, 2023, **324**, 122276.

59 Q. Mu, R. Liu, H. Kimura, J. Li, H. Jiang, X. Zhang, Z. Yu, X. Sun, H. Algadi, Z. Guo, W. Du and C. Hou, Supramolecular self-assembly synthesis of hemoglobin-like amorphous CoP@N, P-doped carbon composites enable ultralong stable cycling under high-current density for lithium-ion battery anodes, *Adv. Compos. Hybrid Mater.*, 2022, **6**, 23–34.

60 X. Luo, G. Yang and D. W. Schubert, Electrically conductive polymer composite containing hybrid graphene nanoplatelets and carbon nanotubes: synergistic effect and tunable conductivity anisotropy, *Adv. Compos. Hybrid Mater.*, 2021, **5**, 250–262.

61 S. Zhang, Z. Jia, B. Cheng, Z. Zhao, F. Lu and G. Wu, Recent progress of perovskite oxides and their hybrids for electromagnetic wave absorption: a mini-review, *Adv. Compos. Hybrid Mater.*, 2022, **5**, 2440–2460.

62 X. Cao, Z. Jia, D. Hu and G. Wu, Synergistic construction of three-dimensional conductive network and double heterointerface polarization via magnetic FeNi for broadband microwave absorption, *Adv. Compos. Hybrid Mater.*, 2022, **5**, 1030–1043.

63 X. Huang, X. Liu, Z. Jia, B. Wang, X. Wu and G. Wu, Synthesis of 3D cerium oxide/porous carbon for enhanced electromagnetic wave absorption performance, *Adv. Compos. Hybrid Mater.*, 2021, **4**, 1398–1412.